inorganics

MDPI

Article

Reversible Sodium Storage of $CoTe_2$ Anode via Lanthanum Doping

Haonan Xie, Xiaolin Xie, Taijiao Guo and Ting Deng *

Key Laboratory of Automobile Materials of MOE, School of Materials Science and Engineering, and Jilin Provincial International Cooperation Key Laboratory of High-Efficiency Clean Energy Materials, Jilin University, Changchun 130012, China; jiexl1621@mails.jlu.edu.cn (X.X.); guotj1621@mails.jlu.edu.cn (T.G.)
* Correspondence: tdeng@jlu.edu.cn

Abstract: Cobalt telluride ($CoTe_2$) is considered an advanced anode material for sodium-ion batteries (SIBs) because of its high theoretical capacity and high conductivity. Nevertheless, the ionic radius of the Co^{2+} ion (0.74 Å) is smaller than that of the Na^+ ion, meaning the integrity of $CoTe_2$ electrodes can be easily damaged when Na^+ ions diffuse into $CoTe_2$ and convert to large Na_2Te. Herein, we propose a doping strategy by introducing an unreactive element but with a large radius to enhance the overall performance. Lanthanum (La) can be doped into the $CoTe_2$ structure to counteract the size effect of Na_2Te since La has a large radius. On the other hand, La with abundant electrons in $CoTe_2$ can also facilitate the charge transfer during charge/discharge. As a result, La-doped $CoTe_2$ (La-$CoTe_2$) can deliver a maximum capacity of 345 mAh g^{-1} at 0.05 A g^{-1} and has a decent rate performance. After 2000 cycles at 2 A g^{-1}, a capacity of 88 mAh g^{-1} remained, which is a notable improvement compared to undoped $CoTe_2$. These results demonstrate the potential of rare earth elements in preparing advanced SIB electrode materials.

Keywords: sodium-ion battery; metal telluride; anode; rare earth element

1. Introduction

Sodium-ion batteries (SIBs) are a promising energy storage technology in the post-lithium era because of their high material reservoir and low cost [1,2]. Most importantly, SIBs share a similar energy storage mechanism with lithium-ion batteries (LIBs), which sheds light on the choice of material for sodium-ion storage. Li^+ and Na^+ ions are very alike, with both having the same outermost electron number [3,4]. The Na^+ ion is a little bit larger than the Li^+ ion in size (ionic radius 1.07 Å vs. 0.76 Å). However, such an ionic radius increase severely restricts sodium-ion storage in traditional graphite anodes and leads to a low specific capacity of 31 mAh g^{-1} [5,6]. In addition, a high reduction potential and slow kinetics can be triggered by the larger ionic radius of the Na^+ ion. Thus, the design and preparation of advanced anode materials are essential for high-performance SIBs.

Metal tellurides have emerged as potential SIB anodes due to the merits of tellurium (Te) [7–10]. Because of the metallic nature of the Te-Te bond, Te exhibits higher electric conductivity (2×10^2 S m^{-1}) than selenium (Se, 1×10^{-4} S m^{-1}) and sulfur (S, 5×10^{-16} S m^{-1}). The large atomic radius and low electronegativity of Te enable facile breaks of metal–Te bonding, thus providing high electron and ion mobility. $CoTe_2$ has drawn much attention because of its large lattice parameters and negligible band gap [11–14]. Nevertheless, the performance stability of $CoTe_2$ anodes is highly compromised by the drastic volume expansion during charge/discharge cycles, leading to a rapidly declining capacity and limited endurance.

check for updates

Academic Editor: Torben R. Jensen

Received: 21 May 2025
Revised: 15 June 2025
Accepted: 18 June 2025
Published: 19 June 2025

Citation: Xie, H.; Xie, X.; Guo, T.; Deng, T. Reversible Sodium Storage of $CoTe_2$ Anode via Lanthanum Doping. *Inorganics* **2025**, *13*, 207. https://doi.org/10.3390/inorganics13060207

Copyright: © 2025 by the authors. Licensee MDPI, Basel, Switzerland. This article is an open access article distributed under the terms and conditions of the Creative Commons Attribution (CC BY) license (https://creativecommons.org/licenses/by/4.0/).

To store Na^+ ions, $CoTe_2$ converts to metallic Co and Te, which further converts to Na_2Te and induces volume expansion. Efforts have been devoted to alleviating this situation, such as compositing $CoTe_2$ with confinement materials and morphology engineering [15,16]. The element doping method is considered an efficient strategy for regulating electrochemical performance as well [17,18]. The ionic radius of the Co^{2+} ion (0.74 Å) is smaller than that of the Na^+ ion, meaning the integrity of $CoTe_2$ electrodes can be easily damaged when Na^+ ions diffuse into $CoTe_2$ and convert to large Na_2Te. Therefore, introducing an element of a large size may strengthen $CoTe_2$ electrodes by counteracting the size effect of Na_2Te. On the other hand, the doping element boosts the redox activity of $CoTe_2$ by providing sufficient electrons and facilitating charge transfer. Under such circumstances, rare earth elements with a large radius and abundant electrons are quite attractive as doping elements to enhance the performance of $CoTe_2$ anodes [19,20]. To the best of our knowledge, no investigation of rare earth element-doped metal tellurides as SIB anodes has been reported.

Herein, lanthanum-doped cobalt ditelluride (La-$CoTe_2$) is synthesized by tellurizing a Co-based metal–organic framework precursor with different La:Co ratios (1:10 and 2:9). La-$CoTe_2$ (1:10) exhibits the best electrochemical performance of the three samples. Specifically, $CoTe_2$ (1:10) can deliver a high specific capacity of 345 mAh g^{-1} at 0.05 A g^{-1} and a decent rate performance (53 mAh g^{-1} at 5 A g^{-1}). Compared to pure $CoTe_2$, the cycling stability is notably enhanced by the introduction of La. After 2000 cycles at 2 A g^{-1}, a capacity of 88 mAh g^{-1} remains. The X-ray diffraction (XRD) indicates that the crystal structure of $CoTe_2$ is preserved, but reactivity and charge transfer are notably improved because of the abundant electrons of La, as evidenced by electrochemical impedance spectroscopy (EIS) analysis. Our work demonstrates the positive contribution of La^{3+} to the Na^+ ion storage ability of metal tellurides and inspires more investigations in the rare earth field.

2. Experimental Section

Material synthesis: For ZIF-67, 249 mg 2-methylimidazole (analytical reagent (AR), Aladdin Reagent (Shanghai) Co., Ltd., Shanghai, China) and 328 mg $Co(NO_3)_2$ (analytical reagent (AR), ≥99.0%, Aladdin Reagent (Shanghai) Co., Ltd.) were dissolved in 25 mL methanol. The two solutions were mixed under stirring to obtain a purple solution. After 24 h of precipitation, a purple solid was obtained by centrifuging the mixed solution, which was further washed and dried in a 60-degree oven overnight. For La-ZIF-67, $La(NO_3)_3$ (analytical reagent (AR), ≥99.0%, Aladdin Reagent (Shanghai) Co., Ltd.) and $Co(NO_3)_2$ with different mole ratios (1:10 (78 mg $La(NO_3)_3$ and 328 mg $Co(NO_3)_2$) and 2:9 (173 mg $La(NO_3)_3$ and 328 mg $Co(NO_3)_2$)) were dissolved in 25 mL methanol; the rest of the synthesis process was the same as that for preparing ZIF-67.

For $CoTe_2$, La-$CoTe_2$ (1:10) and La-$CoTe_2$ (2:9), ZIF-67 (La-ZIF-67) and tellurium powder (Te, analytical reagent (AR), ≥99.0%, Aladdin Reagent (Shanghai) Co., Ltd.) were placed into a tube furnace. The mass ratio of ZIF-67 precursor (100 mg) to Te powder (400 mg) was 1:4. The tube furnace was heated to 600 °C with a heating rate of 5 °C under N_2 atmosphere for 4 h.

Physical characterization: The X-ray diffraction analysis of $CoTe_2$, La-$CoTe_2$ (1:10) and La-$CoTe_2$ (2:9) was carried out using a Bruker D8 powder diffractometer with a LynxEye XE-T detector. Scanning electron microscopy and transmission electron microscopy were conducted using a Hitachi SU8000 scanning electron microscope and JEM ARM 1300S, respectively. X-ray photoelectron spectroscopy and the measurement of N2 isotherms were conducted using the Thermo ESCALAB 250Xi instrument and auto JW-BK132F instrument from JWGB SCI. & TECH instruments.

Electrochemical characterization: The electrochemical performance was assessed in CR2032-type coin cells, in which $CoTe_2$, La-$CoTe_2$ (1:10) and La-$CoTe_2$ (2:9) served as working electrodes, while a sodium metal plate and a glass fiber membrane acted as the counter electrode and separator. Here, 1 M $NaClO_4$ (12.2 mg, analytical reagent (AR), Aladdin Reagent (Shanghai) Co., Ltd.) was dissolved in an ethylene carbonate/diethyl carbonate (EC:DEC = 1:1 Vol%) solution (10 mL) as the electrolyte. To prepare the working electrode, $CoTe_2$ (La-$CoTe_2$), super P and CMC-Na were mixed in distilled water in the mass ratio of 8:1:1 (80 mg:10 mg:10 mg). They were stirred for 10 h to obtain a homogeneous slurry, which was coated onto a copper foil current collector. After being placed in a vacuum oven at 60 °C overnight, the working electrode was prepared. The average mass loading was ~1 mg cm^{-2}. The NEWARE testing system was utilized for charge/discharge profiles under the voltage range of 0.01–3.0 V. A cyclic voltammogram (CV) test and an electrochemical impedance spectroscopy (EIS) test were carried out using a CHI660 electrochemistry workstation.

3. Results and Discussion

La-$CoTe_2$ polyhedrons were prepared by sacrificing the ZIF-67 precursor, as illustrated in Figure 1A. ZIF-67 is a polyhedral metal–organic framework containing Co^{2+} and organic linkers. We chose ZIF-67 as the precursor not only because of its morphology, but also because of its tunable chemical composition, allowing for an easy introduction of La into the precursor. La-ZIF-67 precursors were prepared by a coprecipitation method in MeOH solution containing 2-methylimidazole, La and Co nitrates. Then, the La-ZIF-67 precursor and tellurium powder were placed in a 500 °C tube furnace in a N_2 atmosphere for tellurization, after which La-$CoTe_2$ was obtained. Figure 1B shows the scanning electron microscopy (SEM) image of La-ZIF-67 with a polyhedron morphology. The size of La-ZIF-67 is about 600~800 nm. After tellurization, the purple La-ZIF-67 turned black and the polyhedron morphology become porous, as shown in Figure 1C. Transmission electron microscopy (TEM) confirmed the porosity after tellurization (Figure 1D). The element distribution in La-$CoTe_2$ was analyzed by energy-dispersive spectroscopy (EDS) mapping, from which it could be seen that Co, Te and La were evenly distributed in the sample (Figure 1E).

Figure 2A displays the high-resolution transmission electron microscopy (HRTEM) image of La-$CoTe_2$ (2:9). The irregular light regions represent the pore structures in La-$CoTe_2$. The lattice fringe was calculated as 0.174 nm, corresponding to d_{111}-spacing. Figure 2B exhibits the X-ray diffraction (XRD) patterns of pure $CoTe_2$, La-$CoTe_2$ (1:10) and La-$CoTe_2$ (2:9). From the tellurization of the pure ZIF-67, the peaks at 31.9°, 43.4° and 46.5° can be indexed to the (111), (211) and (002) planes (PDF card No.89-2091), indicating the successful synthesis of $CoTe_2$. Figure S1 shows the XRD pattern of ZIF-67 observed in Figure 2B, indicating the removal of ZIF-67. The lattice parameters *a*, *b* and *c* of $CoTe_2$ are 5.327, 6.322 and 3.900 Å, respectively. After La introduction, the main peaks are well preserved, while the crystallinity of La-$CoTe_2$ (1:10) is reduced, as suggested by the decreased peak intensity. The crystallinity is further reduced as the ratio of La:Co increases to 2:9. This is due to the long-range-ordered structure of $CoTe_2$ being compromised by the La element with a large size. In addition, the size effects of the La element on the surface area and pore structure were investigated by nitrogen adsorption/desorption. The Brunauer–Emmett–Teller (BET) surface area of pure $CoTe_2$ was calculated to be 90.928 m^2 g^{-1} (Figure 2C). After La introduction, the BET surface area decreased to 34.296 m^2 g^{-1} (Figure 2D). Accordingly, the pore width and volume were reduced as well because of the large space occupation of the La atoms (Figure 2E).

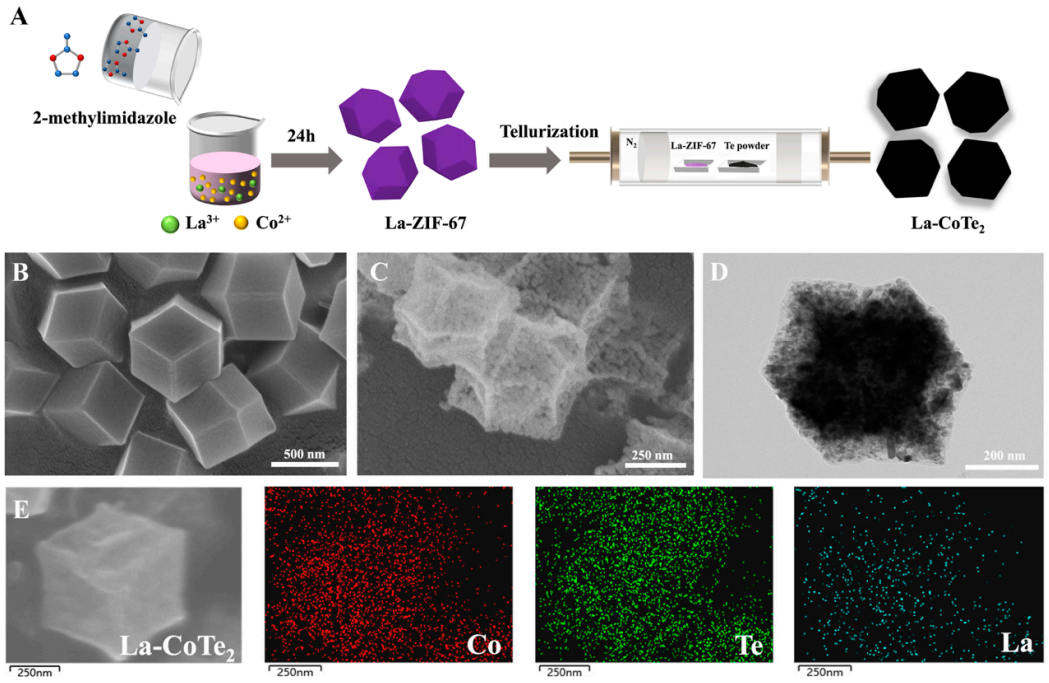


Figure 1. Schematic illustration of La-$CoTe_2$ synthesis and characterization. (**A**) Preparation process of La-$CoTe_2$. (**B**,**C**) SEM images of ZIF precursor and La-$CoTe_2$. (**D**) TEM image of La-$CoTe_2$. (**E**) EDS element mapping of La-$CoTe_2$.

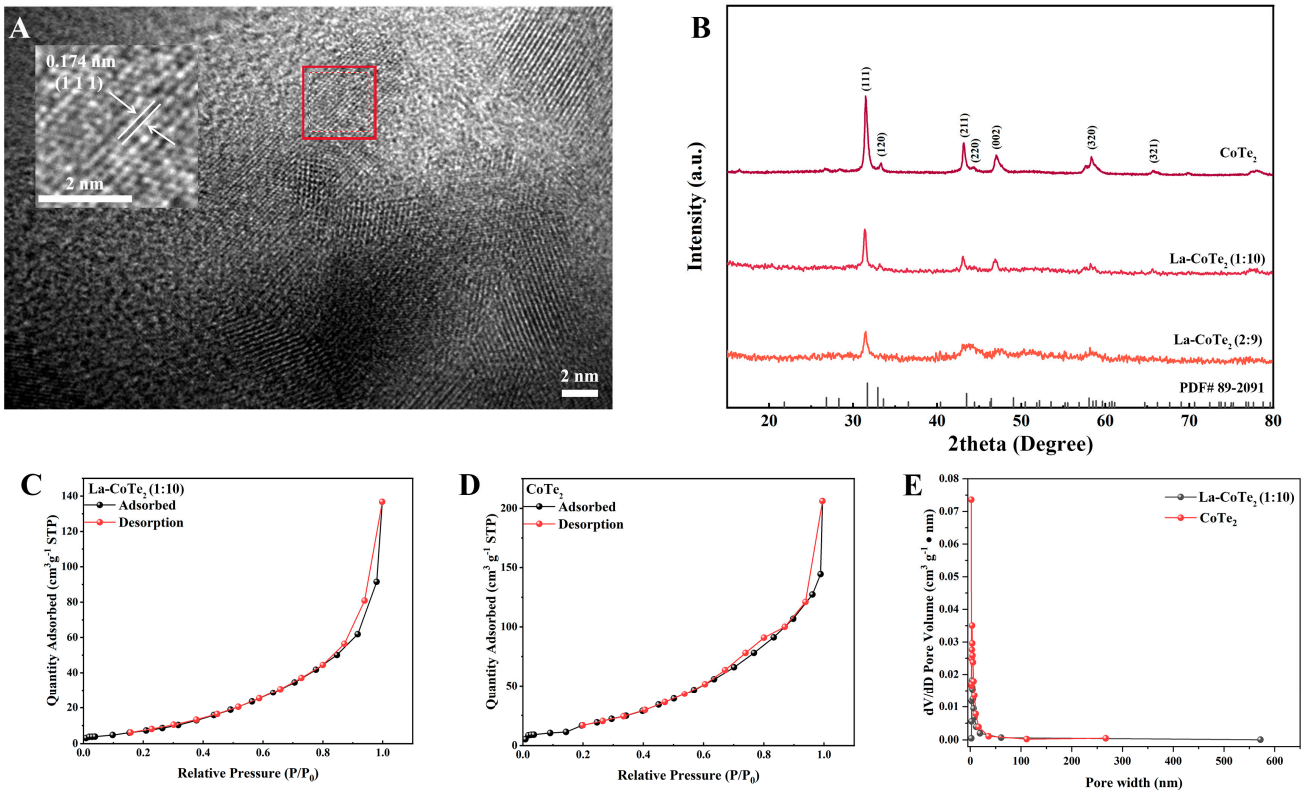


Figure 2. Physical characterization. (**A**) HRTEM image of La-$CoTe_2$ (1:10). (**B**) XRD patterns of $CoTe_2$, La-$CoTe_2$ (1:10) and La-$CoTe_2$ (2:9). (**C**,**D**) N_2 isotherms of La-$CoTe_2$ (1:10) and pure $CoTe_2$. (**E**) Pore width comparison of La-$CoTe_2$ (1:10) and pure $CoTe_2$.

To examine the chemical surface state of La-$CoTe_2$, X-ray photoelectron spectroscopy (XPS) measurement was conducted (Figure 3A). C and N elements were detected in La-$CoTe_2$ because the organic linker (2-methylimidazole) contains carbon and nitrogen. The

La 3d spectrum is shown in Figure 3B; the typical peaks of La 3d indicate that the valence of La is +3 [21,22]. Figure S2 shows the Co 2p XPS spectrum of pure $CoTe_2$, and the two peaks located at 797.4 and 780.2 eV correspond to the Co $2p_{1/2}$ and Co $2p_{3/2}$ of $CoTe_2$, which is indicative that the valence of Co species is +2 [12]. After La introduction, the Co $2p_{1/2}$ and Co $2p_{3/2}$ peaks of La-$CoTe_2$ are centered at 797.2 and 780.3 eV, implying that the electron structure of Co species is not affected by La^{3+} (Figure 3C). Figure 3D reveals that Te $3d_{5/2}$ and Te $3d_{3/2}$ are located around 572.3 and 582.6 eV, quite similar to the undoped $CoTe_2$ sample (Figure S3). In addition, Co-Te-O and La-Te-O bonds were also detected. This is because the Te element of La-$CoTe_2$ can be easily oxidized by oxygen in the air [23].

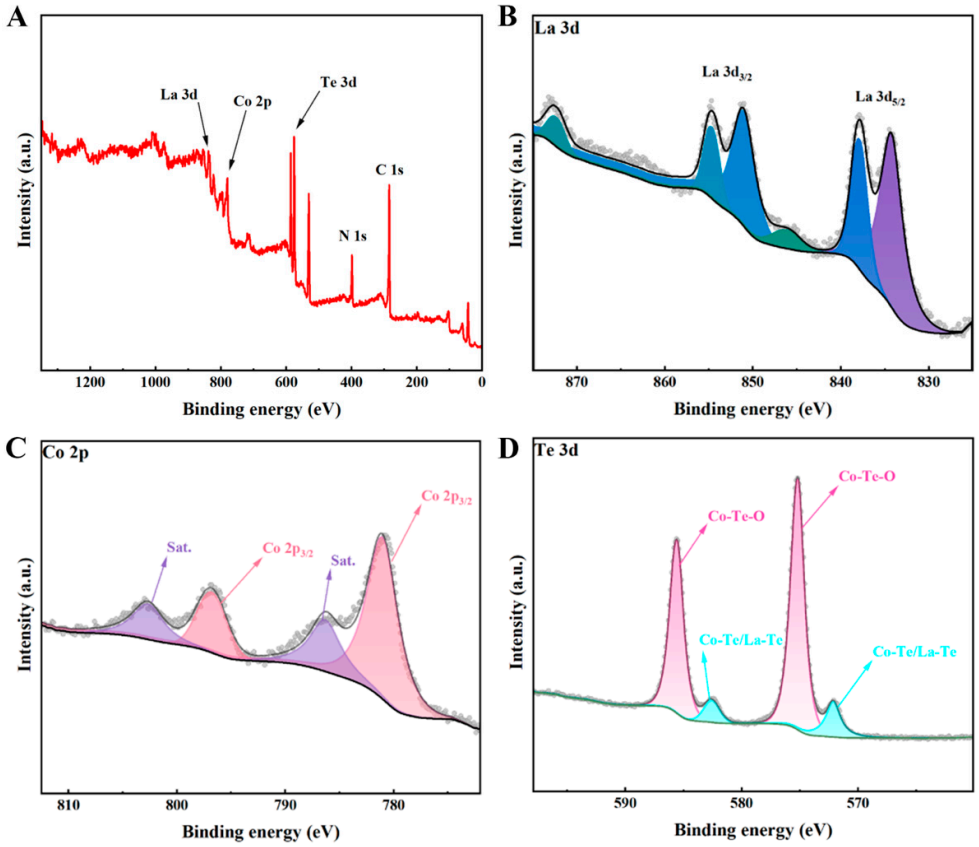


Figure 3. XPS analysis of La-$CoTe_2$. (**A**) Survey spectrum of La-$CoTe_2$. (**B**) La 3d XPS spectrum. (**C**) Co 2p XPS spectrum of La-$CoTe_2$. (**D**) Te 3d XPS spectrum.

The electrochemical performance of pure $CoTe_2$, La-$CoTe_2$ (1:10) and La-$CoTe_2$ (2:9) as SIB anodes was evaluated in CR2032-type coin cells, in which a Na plate acted as the counter and reference electrodes. Figure 4A–C display the discharge capacity of pure $CoTe_2$, La-$CoTe_2$ (1:10) and La-$CoTe_2$ (2:9) at different current densities. One can see that the initial discharge capacities of $CoTe_2$, La-$CoTe_2$ (1:10) and La-$CoTe_2$ (2:9) were much higher than the subsequent cycle; this resulted from the formation of an SEI layer in the electrode/electrolyte surface. After the first cycle, the undoped $CoTe_2$ can deliver a maximum discharge capacity of 275 mAh g^{-1} at a current of 0.05 A g^{-1}. By contrast, the discharge capacity of La-$CoTe_2$ (1:10) at the same current density can reach 345 mAh g^{-1}, indicating that the La element has a positive effect in enhancing the capacity. Furthermore, as the ratio of La:Co increased to 2:9, the maximum capacity dropped to 252 mAh g^{-1}, suggesting that the doping content is also crucial to the performance. Due to the sufficient electrons in La^{3+}, introducing La^{3+} into the $CoTe_2$ structure can boost the activity of the surrounding $CoTe_2$ by enhancing the conductivity. On the other hand, La^{3+} is inactive in Na^+ ion storage, meaning that excessive La^{3+} in the structure can reduce the content of

active $CoTe_2$, leading to a low specific capacity. In addition, one can see that the specific capacities at 5 A g^{-1} of pure $CoTe_2$, La-$CoTe_2$ (1:10) and La-$CoTe_2$ (2:9) were nearly the same, also suggesting that the conductivity and rate capability of $CoTe_2$ were enhanced by La^{3+} introduction. The performance stability of pure $CoTe_2$, La-$CoTe_2$ (1:10) and La-$CoTe_2$ (2:9) was also tested. Figure 4D shows the cycling performance of pure $CoTe_2$ at a current of 2 A g^{-1}. The capacity of pure $CoTe_2$ decayed from 98 mAh g^{-1} to 66 mAh g^{-1} before 800 cycles. Obviously, there was a big capacity drop after 800 cycles. After 1200 cycles, a capacity of 47 mAh g^{-1} remained. The same phenomenon was also observed in other cells with a pure $CoTe_2$ anode (Figure S4). This was probably due to pulverization of the electrode material induced by the huge volume expansion. By contrast, La-$CoTe_2$ (1:10) could stably cycle 2000 times (Figure 4E) and delivered a capacity of 88 mAh g^{-1}. The ionic radius of La^{3+} is 1.06 Å, comparable to that of the Na^+ ion (1.07 Å), meaning that the unreactive large La^{3+} in the $CoTe_2$ structure can counteract the volume expansion derived from Na_2Te formation, resulting in enhanced stability. On the other hand, no sudden capacity drop was observed in La-$CoTe_2$ (2:9), indicating that the whole structure was stabilized by La^{3+}. But after 2000 cycles, a capacity of 51 mAh g^{-1} remained (Figure 4F), which is in accordance with the capacity comparison of pure $CoTe_2$ and La-doped $CoTe_2$ (Figure 4A–C) and suggests that moderate La^{3+} is essential to the overall performance.

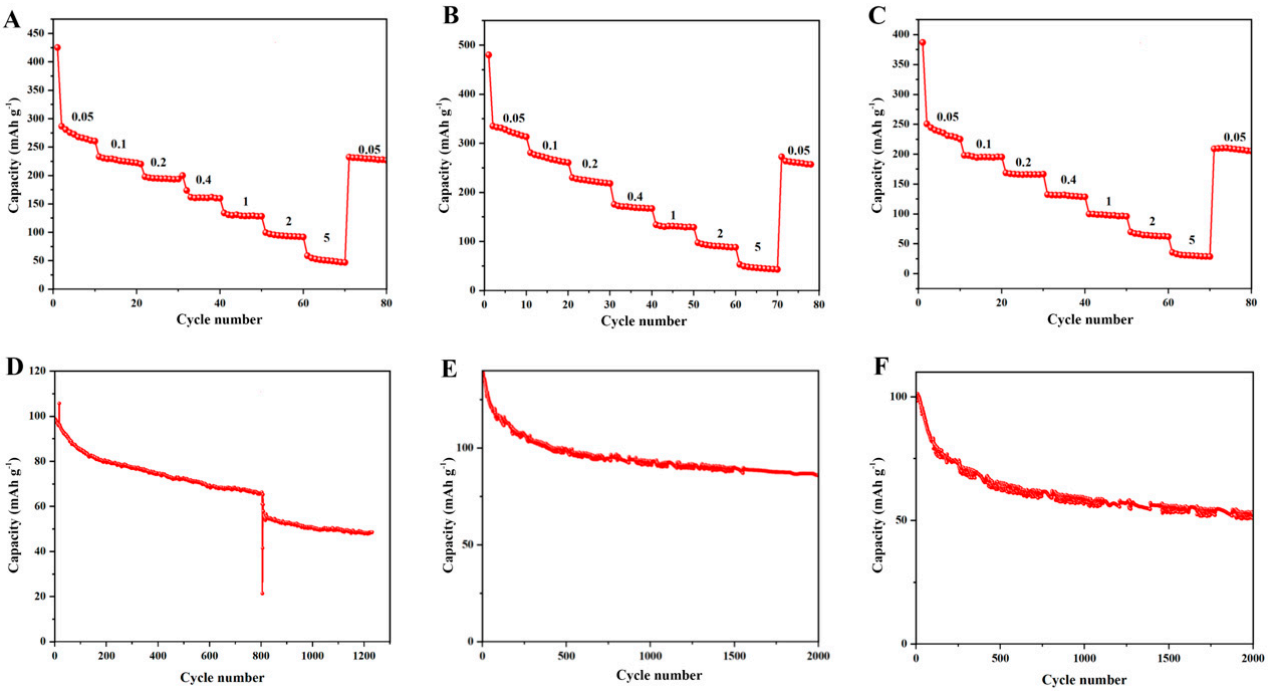


Figure 4. Electrochemical performance analysis. (**A**–**C**) Rate performance of $CoTe_2$, La-$CoTe_2$ (1:10) and La-$CoTe_2$ (2:9). (**D**–**F**) Cycling performance of $CoTe_2$, La-$CoTe_2$ (1:10) and La-$CoTe_2$ (2:9) at current density of 2 A g^{-1}.

To investigate the effect of La^{3+}, electrochemical impedance spectroscopy (EIS) at different cycle depths was conducted on pure $CoTe_2$ and La-$CoTe_2$ (1:10) (Figure 5A,B). The inset is the equivalent circuit, in which R_{ct} and R_s stand for the charge-transfer resistance and series resistance, respectively. The fitted results are summarized in Table S1. The R_{ct} value of pure $CoTe_2$ was calculated to be 890.1 Ω, which is much higher than that of La-$CoTe_2$ (1:10) (676.4 Ω), indicating that the conductivity was notably enhanced by La^{3+} introduction. As the cycle depth increased, the R_{ct} value of pure $CoTe_2$ gradually increased as well, which was probably because of the huge volume expansion and the formation of pulverized materials. Meanwhile, the R_{ct} value of $CoTe_2$ (1:10) decreased as the cycle

depth increased. In addition, the morphology of pure $CoTe_2$ after 200 cycles is shown in Figure 5A's inset, which shows a large crack in the middle. By contrast, the polyhedron morphology was preserved and no crack was observed in La-$CoTe_2$ (1:10) (the inset of Figure 5B), suggesting that La^{3+} stabilized the structure and prevented crack formation. To investigate the reaction kinetics in La-$CoTe_2$ (1:10), cyclic voltammetry (CV) at different scan rates ranging from 0.1 to 1 mV s^{-1} was carried out (Figure 5C). There is a pair of redox peaks corresponding to the plateaus in the charge/discharge profiles. The reaction mechanism of the $CoTe_2$ electrode can be described as follows:

$$CoTe_2 + 4Na^+ + 4e^- \Leftrightarrow Co + 2Na_2Te$$

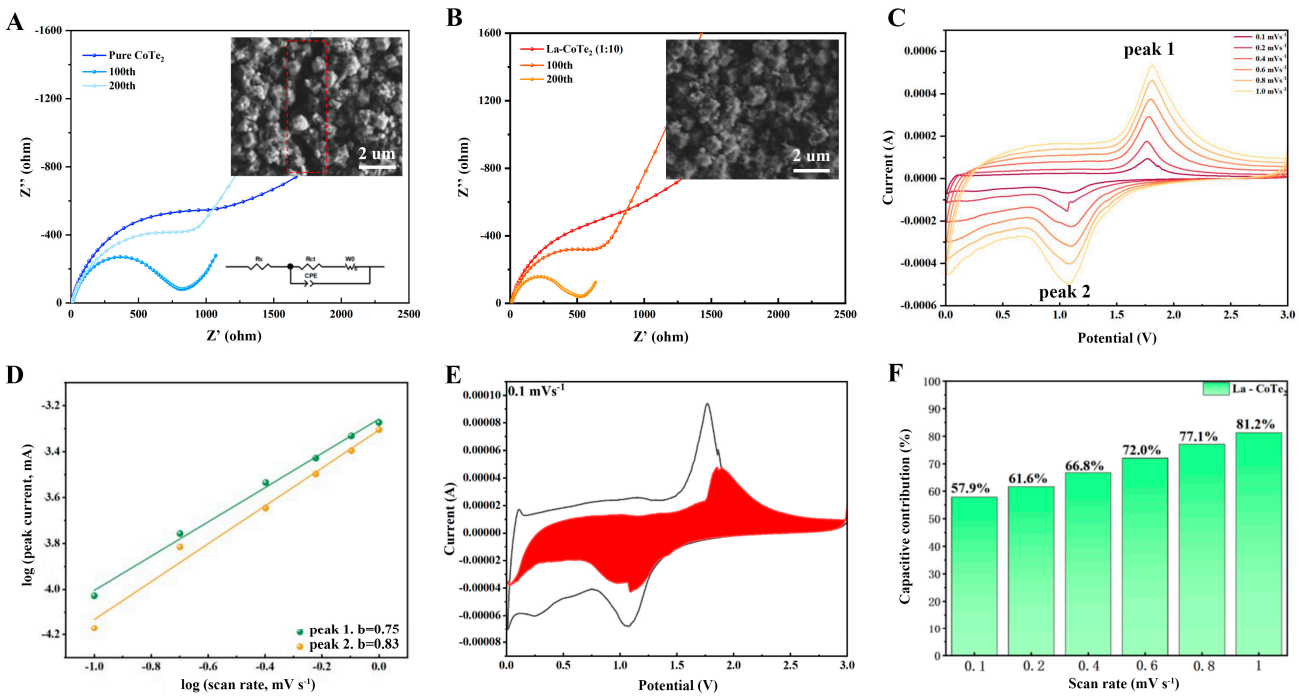


Figure 5. Kinetics evaluation of La-$CoTe_2$. (**A**,**B**) Nyquist plots of $CoTe_2$ and La-$CoTe_2$ (1:10) at different cycle depths; the insets are the equivalent circuit and SEM images of cycled $CoTe_2$ and La-$CoTe_2$ (1:10). (**C**) CV curves of La-$CoTe_2$ (1:10) at different scan rates. (**D**) The log*v* vs. log*i* plot. (**E**) Surface-controlled capacitance at 0.1 mV s^{-1}. (**F**) Capacity contribution of surface-controlled process.

In the charge process, $CoTe_2$ firstly converts metallic Co and Te. Then, Te reacts with the Na^+ ion to form Na_2Te. In the discharge process, Na_2Te converts back to Te to release the Na^+ ion. And the metallic Co reacts with Te to form $CoTe_2$. The redox peaks show no obvious shifts as the scan rate increases, which indicates small surface polarization and excellent redox reversibility. Based on these CV curves, the surface- and diffusion-controlled capacity can be determined according to the following equations:

$$i = av^b$$

$$\log i = b\log v + \log a$$

where the b value stands for the slope of the "log i vs. log v" plot. The b values of the anodic and cathodic peaks are 0.75 and 0.83 (Figure 5D), suggesting that the discharge reaction was controlled by both surface and diffusion processes. As the scan rate increased, the proportion of surface-controlled contribution increased as well (Figures 5E and S5–S9). The percentage reached 81.2% when the scan rate was 1 mV s^{-1}, indicating excellent rate performance (Figure 5F). All these results suggest that the effect of La^{3+} doping is two-fold.

First, the specific capacity is increased. La^{3+} with sufficient electrons can boost the activity of ambient $CoTe_2$ by increasing the conductivity, as proved by the charge/discharge profiles and EIS analysis. Second, the structure stability of $CoTe_2$ is strengthened by La^{3+}, since the unreactive La^{3+} has a large ionic radius, which can counteract the huge volume expansion derived from Na_2Te formation and thus avoid pulverization.

4. Conclusions

To summarize, we propose a doping strategy by introducing the La element with a large radius to counteract the size effect of Na_2Te. On the other hand, La with abundant electrons in $CoTe_2$ can also facilitate the charge transfer during charge/discharge. La-doped $CoTe_2$ was successfully synthesized by sacrificing the ZIF-67 precursor. La-$CoTe_2$ (2:9) shows excellent electrochemical performance as an SIB anode, showing a maximum capacity of 345 mAh g^{-1} at 0.05 A g^{-1} and a decent rate performance. After 2000 cycles at 2 A g^{-1}, a capacity of 88 mAh g^{-1} remained, representing a notable improvement compared with the undoped $CoTe_2$. The introduction of moderate La^{3+} not only counteracts the volume expansion due to its large ionic radius, but also enhances the conductivity by providing sufficient electrons. All these results demonstrate the potential of rare earth elements in preparing advanced SIB electrode materials.

Supplementary Materials: The following supporting information can be downloaded at https://www.mdpi.com/article/10.3390/inorganics13060207/s1: Figure S1: XRD pattern of ZIF-67; Figure S2: Co 2p XPS spectrum of undoped $CoTe_2$; Figure S3: Te 3d XPS spectrum of undoped $CoTe_2$; Figure S4: Cycling performance of pure $CoTe_2$ at the current density of 2 A g^{-1}; Figure S5: Surface-controlled capacitance at 0.2 mV s^{-1}; Figure S6: Surface-controlled capacitance at 0.4 mV s^{-1}; Figure S7: Surface-controlled capacitance at 0.6 mV s^{-1}; Figure S8: Surface-controlled capacitance at 0.8 mV s^{-1}; Figure S9: Surface-controlled capacitance at 1 mV s^{-1}; Table S1: The fitting values of EIS measurements.

Author Contributions: Conceptualization, H.X., X.X., T.G., T.D.; funding acquisition, T.D.; investigation, H.X., X.X., T.G.; resources, T.D.; supervision, T.D.; validation, H.X., X.X., T.G.; visualization, H.X., X.X., T.G.; writing—original draft, H.X., X.X., T.G.; writing—review and editing, T.D. All authors have read and agreed to the published version of the manuscript.

Funding: This work was supported by the 2024 Innovation-High-tech Industry Program of Jilin Province Development and Reform Commission (No. 2024C018-8), the Fundamental Research Funds for the Central Universities, JLU, and "Double-First Class" Discipline for Materials Science & Engineering.

Institutional Review Board Statement: Not applicable.

Informed Consent Statement: Not applicable.

Data Availability Statement: The data presented in this study are available on request from the corresponding author. The data are not publicly available due to data protection.

Conflicts of Interest: The authors declare no conflicts of interest. The funders had no role in the design of the study.

References

1. Wan, Y.; Huang, B.; Liu, W.; Chao, D.; Wang, Y.; Li, W. Fast-Charging Anode Materials for Sodium-Ion Batteries. *Adv. Mater.* **2024**, *36*, e2404574. [CrossRef] [PubMed]
2. Che, C.; Wu, F.; Li, Y.; Li, Y.; Li, S.; Wu, C.; Bai, Y. Challenges and Breakthroughs in Enhancing Temperature Tolerance of Sodium-Ion Batteries. *Adv. Mater.* **2024**, *36*, e2402291. [CrossRef] [PubMed]
3. Kumar Prajapati, A.; Bhatnagar, A. A review on anode materials for lithium/sodium-ion batteries. *J. Energy Chem.* **2023**, *83*, 509–540. [CrossRef]
4. Zheng, W.; Liang, G.; Liu, Q.; Li, J.; Yuwono, J.A.; Zhang, S.; Peterson, V.K.; Guo, Z. The promise of high-entropy materials for high-performance rechargeable Li-ion and Na-ion batteries. *Joule* **2023**, *7*, 2732–2748. [CrossRef]

5. Gao, Y.; Zhang, H.; Peng, J.; Li, L.; Xiao, Y.; Li, L.; Liu, Y.; Qiao, Y.; Chou, S.L. A 30-year overview of sodium-ion batteries. *Carbon Energy* **2024**, *6*, e464. [CrossRef]
6. Qiao, S.; Zhou, Q.; Ma, M.; Liu, H.K.; Dou, S.X.; Chong, S. Advanced Anode Materials for Rechargeable Sodium-Ion Batteries. *ACS Nano* **2023**, *17*, 11220–11252. [CrossRef]
7. Zhao, W.; Shi, X.; Liu, B.; Ueno, H.; Deng, T.; Zheng, W. The design and engineering strategies of metal tellurides for advanced metal-ion batteries. *J. Energy Chem.* **2024**, *89*, 579–598. [CrossRef]
8. Kim, M.; Choi, H.-Y.; Yu, S.-H. Recent progress in design strategies for high-performance metal-tellurium batteries. *Chem. Eng. J.* **2025**, *504*, 158528. [CrossRef]
9. Cui, J.; Zheng, H.; Zhang, Z.; Hwang, S.; Yang, X.-Q.; He, K. Origin of anomalous high-rate Na-ion electrochemistry in layered bismuth telluride anodes. *Matter* **2021**, *4*, 1335–1351. [CrossRef]
10. Chen, B.; Zhao, Y.; Yuan, B.; Zhu, Y.; Chong, S. Antimony Telluride as Bifunctional Host Material for Dendrite-Free Sodium Metal Batteries. *Nano Lett.* **2025**, *25*, 4869–4877. [CrossRef]
11. Li, Z.; Yu, F.; Yang, X.; Yang, Y.; Li, X.; Gao, Y.; Wang, L.; Lü, W. FeTe2/CoTe2 heterojunction as anode materials of potassium-ion batteries for improved cycling stability. *Chem. Eng. J.* **2025**, *504*, 159100. [CrossRef]
12. Lu, Z.; Zhang, P.; Li, D.; Yin, F.; Weng, J.; Cong, H. MOF-derived defect-rich CoTe2 confined in graphene aerogel for superior sodium/potassium storage with ultralong lifespan. *Chem. Eng. J.* **2025**, *506*, 159896. [CrossRef]
13. Gong, Q.; Yang, D.; Yang, H.; Wu, K.; Zhang, J.; Bi, W.; Diao, J.; Li, C.; Yu, J.; Zhang, C.Y.; et al. Cobalt Ditelluride Meets Tellurium Vacancy: An Efficient Catalyst as a Multifunctional Polysulfide Mediator toward Robust Lithium-Sulfur Batteries. *ACS Nano* **2024**, *18*, 28382–28393. [CrossRef]
14. Huang, Y.; Li, J.; Zhang, Y.; Lin, L.; Sun, Z.; Gao, G.; Sa, B.; Wang, L.; Ma, L.; Lee, S.; et al. Energizing Robust Sulfur/Lithium Electrochemistry via Nanoscale-Asymmetric-Size Synergism. *J. Am. Chem. Soc.* **2025**, *147*, 4752–4765. [CrossRef] [PubMed]
15. Jiang, Y.; Wu, F.; Ye, Z.; Zhou, Y.; Chen, Y.; Zhang, Y.; Lv, Z.; Li, L.; Xie, M.; Chen, R. Confining CoTe2-ZnTe heterostructures on petal-like nitrogen-doped carbon for fast and robust sodium storage. *Chem. Eng. J.* **2023**, *451*, 138430. [CrossRef]
16. Zhao, W.; Zhang, W.; Lei, Y.; Wang, L.; Wang, G.; Wu, J.; Fan, W.; Huang, S. Dual-Type Carbon Confinement Strategy: Improving the Stability of CoTe2 Nanocrystals for Sodium-Ion Batteries with a Long Lifespan. *ACS Appl. Mater. Interfaces* **2022**, *14*, 6801–6809. [CrossRef]
17. Hayat, A.; Sohail, M.; Alzahrani, A.Y.A.; Ali, H.; Abu-Dief, A.M.; Amin, M.S.; Alenad, A.M.; Al-Mhyawi, S.R.; Al-Hadeethi, Y.; Ajmal, Z.; et al. Recent advances in heteroatom-doped/hierarchical porous carbon materials: Synthesis, design and potential applications. *Prog. Mater. Sci.* **2025**, *150*, 101408. [CrossRef]
18. Patnaik, K.S.; Mantripragada, B.S.; Punyasloka, S.; Matsumi, N. Advancing lithium-ion battery performance with heteroatom-based anode architectures for fast charging and high capacity. *Chem. Commun.* **2025**, *61*, 1282–1302. [CrossRef]
19. Chen, Y.; Li, S.; Li, C.; Leng, X.; Prakash, N.G.; Ko, T.J. Functional La@ZIF-8-enhanced composite quasi-solid electrolyte for high-performance Li-metal batteries. *Chem. Eng. J.* **2025**, *508*, 160932. [CrossRef]
20. Huang, J.; Yu, C.; Li, J.; Xiao, W.; Zhong, J.B.; Shen, P.K.; Tian, Z.Q. Rare-earth lanthanum-nitrogen-carbon enhanced by abundant microspores for efficient oxygen reduction reaction. *J. Energy Chem.* **2025**, *106*, 812–822. [CrossRef]
21. Zhang, X.; Yin, X.; Xie, J.; Wang, M.; Ma, H.; Tang, M.; Cao, Y. Lanthanum-doped Na4Fe3(PO4)2P2O7/C as cathode materials in sodium-ion batteries: Enhanced ion diffusion kinetics and embedded pseudocapacitance. *J. Power Sources* **2025**, *635*, 236531. [CrossRef]
22. Liu, Z.; Wu, Y.; Huo, H.; Jian, J.; Sun, D.; Zhang, X.; Du, C.; Zuo, P.; Yin, G.; Ma, Y. Surface-Phase Engineering via Lanthanum Doping Enables Enhanced Electrochemical Performance of Li-Rich Layered Cathode. *ACS Appl. Energy Mater.* **2022**, *5*, 9648–9656. [CrossRef]
23. Zhao, W.; Mo, L.; Shi, X.; Liu, B.; Yang, G.; Deng, T. Anionic chemistry regulation boosting the reversible redox in CoSexTey@C polyhedrons for sodium storage. *Chem. Eng. J.* **2024**, *492*, 152214. [CrossRef]

Disclaimer/Publisher's Note: The statements, opinions and data contained in all publications are solely those of the individual author(s) and contributor(s) and not of MDPI and/or the editor(s). MDPI and/or the editor(s) disclaim responsibility for any injury to people or property resulting from any ideas, methods, instructions or products referred to in the content.